



HAL
open science

Photocatalytic Performance of Perovskite and Metal–Organic Framework Hybrid Material for the Reduction of N₂ to Ammonia

Masoumeh Chamack, Madjid Ifires, Sayed Ali Akbar Razavi, Ali Morsali, Ahmed Addad, Afsanehsadat Larimi, Sabine Szunerits, Rabah Boukherroub

► **To cite this version:**

Masoumeh Chamack, Madjid Ifires, Sayed Ali Akbar Razavi, Ali Morsali, Ahmed Addad, et al.. Photocatalytic Performance of Perovskite and Metal–Organic Framework Hybrid Material for the Reduction of N₂ to Ammonia. *Inorganic Chemistry*, 2022, 61 (3), pp.1735-1744. 10.1021/acs.inorgchem.1c03622 . hal-03549843

HAL Id: hal-03549843

<https://hal.science/hal-03549843v1>

Submitted on 7 Nov 2022

HAL is a multi-disciplinary open access archive for the deposit and dissemination of scientific research documents, whether they are published or not. The documents may come from teaching and research institutions in France or abroad, or from public or private research centers.

L'archive ouverte pluridisciplinaire **HAL**, est destinée au dépôt et à la diffusion de documents scientifiques de niveau recherche, publiés ou non, émanant des établissements d'enseignement et de recherche français ou étrangers, des laboratoires publics ou privés.

Photocatalytic Performance of the Perovskite and Metal–Organic Framework Hybrid Material for the Reduction of N₂ to Ammonia

Masoumeh Chamack, Madjid Ifires, Sayed Ali Akbar Razavi, Ali Morsali,* Ahmed Addad, Afsanehsadat Larimi,* Sabine Szunerits, and Rabah Boukherroub*



Cite This: <https://doi.org/10.1021/acs.inorgchem.1c03622>



Read Online

ACCESS |



Metrics & More

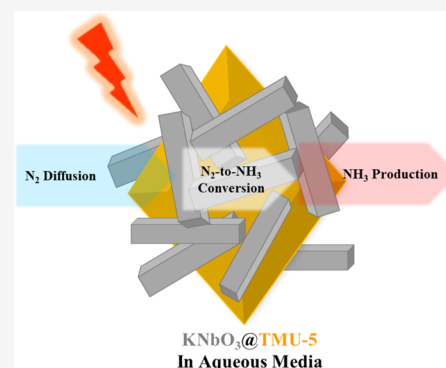


Article Recommendations



Supporting Information

ABSTRACT: The orthorhombic phase of KNbO₃ perovskite has been applied for nitrogen (N₂) photoreduction to ammonia (NH₃). However, this material suffers from a low surface area and low ammonia production efficiency under UV light irradiation. To eliminate these barriers, we used a metal–organic framework (MOF), named as TMU-5 (with formula [Zn(OBA)(BPDH)_{0.5}]_n·1.5DMF, where H₂OBA = 4,4'-oxybis(benzoic acid) and BPDH = 2,5-bis(4-pyridyl)-3,4-diaza-2,4-hexadiene), for the synthesis of the KNbO₃@TMU-5 hybrid material. KNbO₃@TMU-5 achieved a NH₃ production rate of 39.9 μmol·L⁻¹·h⁻¹·g⁻¹ upon UV light irradiation, as compared to 20.5 μmol·L⁻¹·h⁻¹·g⁻¹ recorded for KNbO₃ under similar experimental conditions. Using different characterization techniques especially gas adsorption, cyclic voltammetry, X-ray photoelectron spectroscopy, photocurrent measurements, and Fourier transform infrared spectroscopy, it has been found that the higher photoactivity of KNbO₃@TMU-5 in ammonia production is due to its higher surface area, higher electron–hole separation efficiency, and higher density of negative charges on Nb sites. This work shows that hybridization of conventional semiconductors (SCs) with photoactive MOFs can improve the photoactivity of the SC@MOF hybrid material in different reactions, especially kinetically complex reactions like photoconversion of nitrogen to ammonia.



This work shows that hybridization of conventional semiconductors (SCs) with photoactive MOFs can improve the photoactivity of the SC@MOF hybrid material in different reactions, especially kinetically complex reactions like photoconversion of nitrogen to ammonia.

1. INTRODUCTION

Increasing world population and consequent demand for growing agricultural products have led to an increase in demand for ammonia (NH₃), as it represents a basic building block for fertilizer industry. NH₃ is generally produced through the Haber–Bosch process using pure H₂ and N₂ gases under high temperature (>500 °C) and pressure (>200 bar) conditions. Therefore, industrial-scale production of NH₃ requires consumption of large amounts of fossil fuels. In addition to utilizing a large amount of world's energy, industrial production of NH₃ also emits a lot of greenhouse gases every year.¹ In order to address these issues, the last decade has witnessed a huge increase of investigations on the development of low-cost and sustainable photocatalytic processes for NH₃ production.^{1–4} In the photocatalytic NH₃ production process, N₂ and H₂O react at room temperature and atmospheric pressure to produce ammonia and O₂ under light irradiation.^{1,3} One of the key factors of this process is selecting the appropriate photocatalyst. An ideal photocatalyst for NH₃ production should have some features like facilitated gas diffusion pathway, enhanced adsorption of the reactants, having a band gap energy larger than 1.2 eV with proper band edge position, and activation of molecular nitrogen.^{4,5} Perovskite oxide compounds with the ABO₃ structure play noteworthy roles in various photocatalytic reactions including

water splitting into hydrogen, CO₂ photoreduction into fuels, and degradation of organic pollutants and can be regarded as one of the promising candidates for N₂ fixation reaction.⁶ However, there are only a few reports on this class of materials for the photocatalytic reduction of N₂. In this regard, the only reported perovskite oxide compounds are KNbO₃,^{7,8} LaCoO₃,⁹ SrTiO₃,¹⁰ BiFeO₃,¹¹ LiNbO₃,¹² and layered Bi₂WO₆.^{13,14} Therefore, more investigations are required to understand the aptitude of perovskite oxide materials in the photocatalytic production of NH₃ from N₂.

As a perovskite, KNbO₃ can be regarded as a promising photocatalyst for N₂ photoreduction reaction, owing to its proper conduction and valence band positions. The conduction band (CB) and valence band (VB) of KNbO₃ are located at around –0.8 and +2.39 eV versus standard hydrogen electrode, respectively (<https://doi.org/10.1016/j.apcata.2019.06.001>).^{7,15} However, the band gap of KNbO₃ is in the 3.08–3.24 eV range.¹⁶ Therefore, the best activity for this

Received: November 19, 2021

64 photocatalyst is achieved under UV irradiation. Furthermore,
65 the specific surface area value, recorded for KNbO_3 by means
66 of the N_2 adsorption–desorption technique, is in the range of
67 0.68 to $3.9 \text{ m}^2 \text{ g}^{-1}$.¹⁶ Such a low surface area might be due to
68 the weak interactions between nitrogen gas molecules and the
69 surface atoms of solid KNbO_3 , which restricts its photo-
70 catalytic applicability in N_2 fixation reaction. To address this
71 hurdle, metal/nonmetal ion doping, noble metal loading, and
72 coupling with SCs have been investigated as approaches for
73 tuning the band gap and surface area of perovskite oxides
74 including KNbO_3 .^{7–14}

75 To improve the photocatalytic properties of KNbO_3 , metal–
76 organic frameworks (MOFs) can be appropriate candidates.
77 MOFs, classified as highly porous materials with remarkable
78 potential in adsorption of gas molecules including N_2 , can play
79 important roles in enhancing the capability of photocatalysts in
80 N_2 reduction reactions.¹⁷ However, to date, no investigations
81 highlighting the effect of MOF coupling on the photocatalytic
82 properties of KNbO_3 have been reported. Furthermore, there
83 are still no study about the effect of coupling of MOFs with
84 perovskite oxides on their photocatalytic operation in N_2
85 fixation reactions.⁶ In spite of increasing gas molecule
86 adsorption, MOFs with the appropriate structure can also
87 improve light absorption, charge separation, and reactant
88 activation, which are expected to lead to superior photo-
89 catalytic performance.¹⁸ In this regard, TMU-5
90 ($[\text{Zn}_2(\text{OBA})_2(\text{BPDH})] \cdot (\text{DMF})$) has been described as one
91 of the promising materials with desirable porosity, band gap
92 (2.25 eV) in the visible region, and high specific surface area
93 ($591 \text{ m}^2 \text{ g}^{-1}$ based on N_2 adsorption–desorption analysis).^{19,20}
94 Additionally, it has been demonstrated that coupling of
95 photoactive TMU-5 to MoO_3 (band gap: 3.2 eV) led to
96 improvement of photodegradation of dibenzothiophene over
97 MoO_3 .²⁰

98 In this work, a hybrid material consisting of MOF (TMU-5)
99 and perovskite oxide (KNbO_3) is synthesized and applied as a
100 photocatalyst for N_2 fixation reaction, and the effect of
101 coupling of the MOF on the structural properties and
102 photocatalytic performance of the KNbO_3 perovskite oxide
103 material has been investigated.

2. EXPERIMENTAL SECTION

104 **2.1. Materials and Instrumentation.** *2.1.1. Materials and*
105 *Methods.* Sodium dodecyl sulfate (SDS, $\geq 97\%$), niobium(V) oxide
106 (Nb_2O_5 , 99.9%), potassium hydroxide (KOH, 99.99%), 4,4'-oxy-
107 bisbenzoic acid (oba, 99%), and zinc(II) acetate dihydrate (Zn -
108 $(\text{CH}_3\text{COO})_2 \cdot 2\text{H}_2\text{O}$, $\geq 99.0\%$) were commercially available from
109 Sigma-Aldrich company. Acetonitrile (CH_3CN) and dimethylforma-
110 mide (DMF, $\geq 99.9\%$) were obtained from Merck Company. All
111 materials were used without further purification unless otherwise
112 stated. The ligand 1,4-bis(4-pyridyl)-2,3-diaza-1,3-butadiene (BPDH)
113 was synthesized according to a previously reported method.²¹

114 The synthesized samples were characterized using various analytical
115 tools. X-ray powder diffraction (XRD) measurements were performed
116 using a Philips X'pert diffractometer with monochromated $\text{Cu K}\alpha$
117 radiation. N_2 adsorption–desorption isotherms were measured on a
118 Nova Station A instrument at 77 K . The specific surface area was
119 calculated in accordance to the Brunauer–Emmet–Teller (BET)
120 method. The sample for Raman analysis was prepared by dispersing
121 the sample in ethanol by sonication. $50 \mu\text{L}$ of the solution was drop-
122 cast on a clean silicon wafer and dried. Micro-Raman spectroscopy
123 measurements were recorded on a HORIBA Jobin Yvon LabRam HR
124 micro-Raman system combined with a 473 nm laser diode as the
125 excitation source. Visible light was focused by a $100\times$ objective. The
126 scattered light was collected by the same objective in backscattering

configuration, dispersed by an 1800 mm focal length monochromator, 127
and detected by a charge-coupled device (CCD) camera. Scanning
electron microscopy (SEM) images were recorded by a Hitachi S-
4160 FESEM instrument. Transmission electron microscopy (TEM)
images were acquired on a FEI TITAN Themis 300 operating at 300
kV, equipped with a Schottky FEG electron gun and a
monochromator. Energy-dispersive X-ray spectroscopy (EDX)
analysis was performed with a Philips CM30 microscope operating
at 300 kV and equipped with a Bruker EDX detector. X-ray
photoelectron spectroscopy (XPS) measurements were recorded with
an ESCALAB 220 XL spectrometer from Vacuum Generators,
featuring a monochromatic $\text{Al K}\alpha$ X-ray source (1486.6 eV) and a
spherical energy analyzer operated in the CAE (constant analyzer
energy) mode (CAE = 100 eV for survey spectra and CAE = 40 eV
for high-resolution spectra), using the electromagnetic lens mode. No
flood gun source was needed due to the conducting character of the
substrates. The angle between the incident X-rays and the analyzer
was 58° . The detection angle of the photoelectrons was 30° .

2.2. Synthesis Procedures. *2.2.1. Synthesis of KNbO_3 .* A
reported hydrothermal method was used to prepare the KNbO_3
material.²² In short, 36 g of KOH was dissolved in 80 mL of distilled
water. 1 g of Nb_2O_5 was added to the alkaline solution and stirred at
 50°C for 30 min . Subsequently, 2.88 g of SDS was added to the
mixture and stirred at 50°C for an additional 30 min . The obtained
white color suspension was poured into a 150 mL Teflon-lined
stainless-steel autoclave and heated at 180°C for 48 h . After that, a
white solid was formed, separated by centrifugation, and washed with
distilled water and ethanol. The obtained KNbO_3 powder was dried at
 80°C overnight.

2.2.2. Synthesis of TMU-5. 0.26 g of 4,4'-oxybisbenzoic acid
(H_2OBA) was added to 25 mL of DMF and stirred at 80°C for 30
min. Subsequently, 0.22 g of $\text{Zn}(\text{CH}_3\text{COO})_2 \cdot 2\text{H}_2\text{O}$ and 0.24 g of
BPDH were separately dissolved in 15 mL of DMF. The two solutions
were added to the abovementioned mixture and kept under stirring at
 80°C for 72 h . The obtained yellow powder was washed several times
with DMF and dried at 80°C for 24 h . Finally, the prepared MOF
was activated by washing it several times with acetonitrile and dried at
 120°C for 72 h . Scheme S1 depicts the structure of TMU-5.

2.2.3. Synthesis of $\text{KNbO}_3@$ TMU-5. The co-precipitation
method was used for the synthesis of the $\text{KNbO}_3@$ TMU-5
composite. 1 g of KNbO_3 powder was added to 50 mL of DMF
and sonicated for 5 min . Afterward, 0.5 g of H_2OBA was added to the
suspension and the resulting mixture was stirred (500 rpm) at 80°C
for 30 min . Subsequently, 0.44 g of $\text{Zn}(\text{CH}_3\text{COO})_2 \cdot 2\text{H}_2\text{O}$ and 1 g of
BPDH, separately dissolved in 20 mL of DMF, were added to the
mixture and the reaction pot was completely sealed. The mixture was
stirred at 80°C for 72 h . The obtained pale yellowish powder was
separated by centrifugation, washed several times with DMF, and
dried at 80°C for 24 h . Finally, this sample was activated by the same
method as applied for TMU-5. The scheme of the synthesis method is
depicted in Scheme S2.

2.3. Preparation of the Modified Electrode. 1 mg of $\text{KNbO}_3@$
TMU-5 powder was dispersed in $100 \mu\text{L}$ of ethanol using an
ultrasonic bath for 10 min . $3 \mu\text{L}$ of the dispersed mixture was dripped
on the glassy carbon (2 mm diameter) electrode surface and allowed
to dry under the IR lamp. Then, $1 \mu\text{L}$ of nafion solution was added on
to the surface and allowed it to dry by the same method. The counter
electrode and reference electrode were platinum disk (2 mm
diameter) and calomel electrodes, respectively. 10 mL of Na_2SO_4
(0.2 M) was used as the electrolyte solution.

2.4. N_2 Photoreduction Test. *2.4.1. General Photocatalytic*
Process. The nitrogen (N_2) photoreduction experiments were
performed in a quartz tube. 10 mg of the photocatalyst was added
to 10 mL of water and 0.789 mL of ethanol as a hole scavenger. The
mixture was dispersed using an ultrasonicator for 10 min , and the
resulting suspension was saturated with N_2 . During photoreduction
under UV irradiation (power of lamp (P) = 0.2 W), N_2 was bubbled
into the solution. At certain time intervals, 2 mL of the reaction
mixture was collected and immediately centrifuged to separate the
liquid sample from the solid catalyst. The concentration of NH_3 was 196

197 measured using the indophenol method via UV–vis absorption
 198 spectra recorded using a Safas Bio-UVmc² spectrophotometer in
 199 quartz cuvettes with an optical path of 10 mm. The wavelength range
 200 was 200–800 nm.²³ UV–vis curves of indophenol assays with NH₄⁺
 201 ions and the calibration curve used for estimation of NH₃ by NH₄⁺
 202 ion concentration are illustrated in Figure S1.

203 2.4.2. Photocatalytic Stability of KNbO₃@TMU-5. The cycling
 204 stability of the KNbO₃@TMU-5 photocatalyst for N₂ reduction was
 205 assessed under UV irradiation. After each cycle, the catalyst was
 206 collected by centrifugation, dried in the oven at 60 °C overnight, and
 207 reused in the subsequent experiment.

3. RESULTS AND DISCUSSION

208 3.1. Characterization of Materials. Different instrumen-
 209 tal techniques including powder X-ray diffraction (PXRD),
 210 nitrogen adsorption at 77 K, XPS, transmission electron
 211 spectroscopy (TEM), Fourier transform infrared spectroscopy
 212 (FT-IR), Raman spectroscopy, and SEM were applied to
 213 characterize the structure of KNbO₃@TMU-5.

214 Combination of PXRD patterns for KNbO₃@TMU-5 and
 215 its components clearly shows that the structure of both
 216 components is identical in their pristine and composite
 217 materials (Figure 1). In detail, the PXRD pattern of the

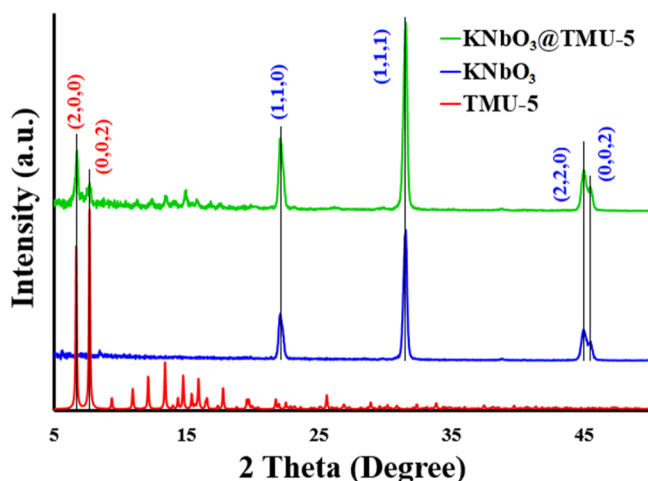


Figure 1. Combination of PXRD patterns of KNbO₃@TMU-5 and the components.

218 TMU-5 MOF comprises two sharp peaks centered at 6.7 and
 219 7.6° indexed respectively to (2,0,0) and (0,0,2) miller indices,
 220 which are present in the composite. Also, other relatively
 221 weaker bands at $2\theta = 12\text{--}16^\circ$ for the TMU-5 sample (12.1,
 222 13.4, 14.7, and 15.9° assigned to (1,1,1), (1,1,-2), (3,1,0), and
 223 (3,1,-2), respectively) are observable in the composite. For
 224 the KNbO₃ sample, XRD peaks observed at 22.1, 31.5, 44.9,
 225 and 45.5° are respectively indexed to (1,1,0), (1,1,1), (2,2,0),
 226 and (0,0,2) planes of the orthorhombic phase of KNbO₃
 227 (space group *Amm*2) (JCPDS card 32-0822),¹⁶ which are
 228 observable in the composite, too.

229 To investigate the role of TMU-5 species in supplying the
 230 N₂ reactant for efficient utilization of photoinduced electrons
 231 in KNbO₃, N₂ adsorption capability of samples was assessed by
 232 nitrogen adsorption–desorption measurement at 77 K (Figure
 233 2). For the KNbO₃ sample, an isotherm of type III is recorded,
 234 which is consistent with nonporous or macroporous solids.²⁴
 235 For the KNbO₃@TMU-5 composite, an isotherm of type I(a)
 236 corresponding to microporous materials having mainly narrow
 237 micropores (width < ~1 nm) is observed.²⁴ The BET surface

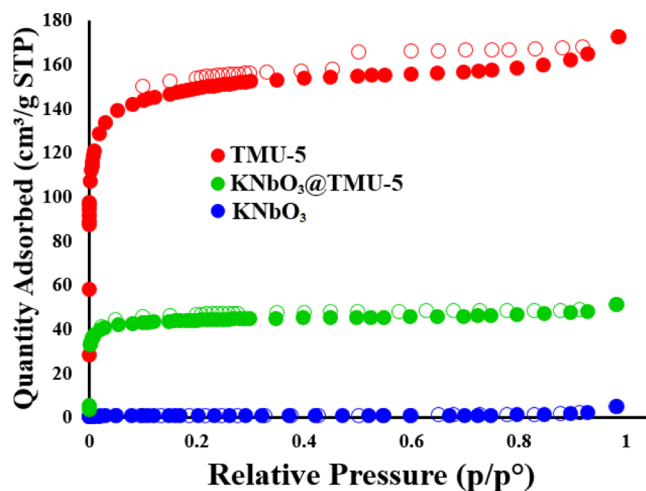


Figure 2. Nitrogen adsorption at 77 K for the KNbO₃@TMU-5 composite and its components.

238 areas, calculated from nitrogen adsorption–desorption iso-
 239 therms, are about 2 and 172 m²·g⁻¹ for KNbO₃ and KNbO₃@
 240 TMU-5 samples, respectively. Therefore, compared to pristine
 241 KNbO₃, the adsorption capacity of the KNbO₃@TMU-5
 242 hybrid material for adsorption of N₂ gas molecules was
 243 significantly increased. This is a structurally critical improve-
 244 ment for observation enhancement in photocatalytic efficiency
 245 of KNbO₃@TMU-5 compared to pristine KNbO₃, and it can
 246 be concluded that TMU-5 can act like a gas cylinder for N₂
 247 storage. TMU-5 can adsorb and store N₂ gas molecules and
 248 inject them to the SC surface where the photocatalytic reaction
 249 occurs.

250 XPS was performed to investigate the elemental composition
 251 and electronic state of the KNbO₃ surface atoms before and
 252 after coupling with TMU-5. The full-scan XPS spectra of
 253 KNbO₃, TMU-5, and KNbO₃@TMU-5 are displayed in
 254 Figure 3. The XPS spectrum of KNbO₃ confirms the presence of

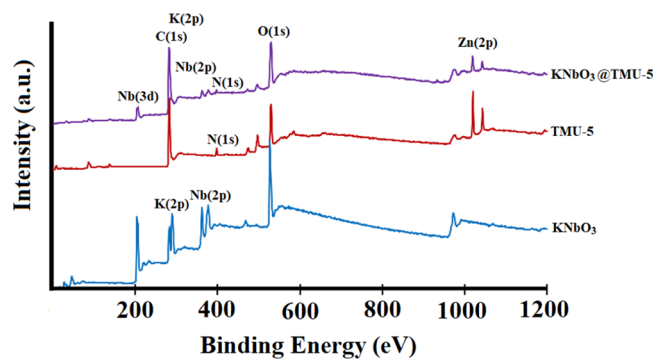


Figure 3. Full-scan XPS spectra of KNbO₃, TMU-5, and KNbO₃@TMU-5.

255 potassium, niobium, and oxygen elements. The XPS spectrum
 256 of TMU-5 shows the presence of zinc, carbon, oxygen, and
 257 nitrogen corresponding to metal ions and linker organic
 258 ligands of the MOF. For the KNbO₃@TMU-5 spectrum, all
 259 peaks related to component elements of both KNbO₃ (K, Nb,
 260 and O) and TMU-5 (Zn, C, N, and O) are observed.

261 Besides XPS analysis for KNbO₃@TMU-5 and its
 262 components, SEM and TEM analyses have been applied to
 263 elucidate the morphological structure and structural composi-

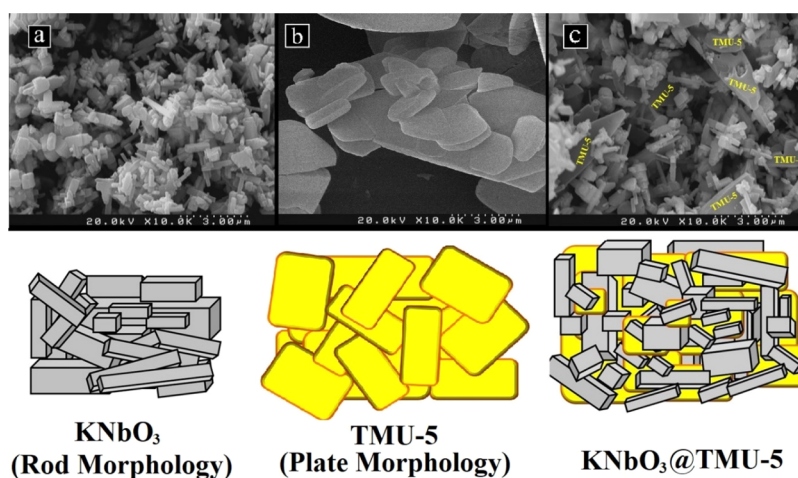


Figure 4. SEM images of KNbO_3 , TMU-5, and $\text{KNbO}_3@TMU-5$. The schemes given below illustrate the morphology of the materials.

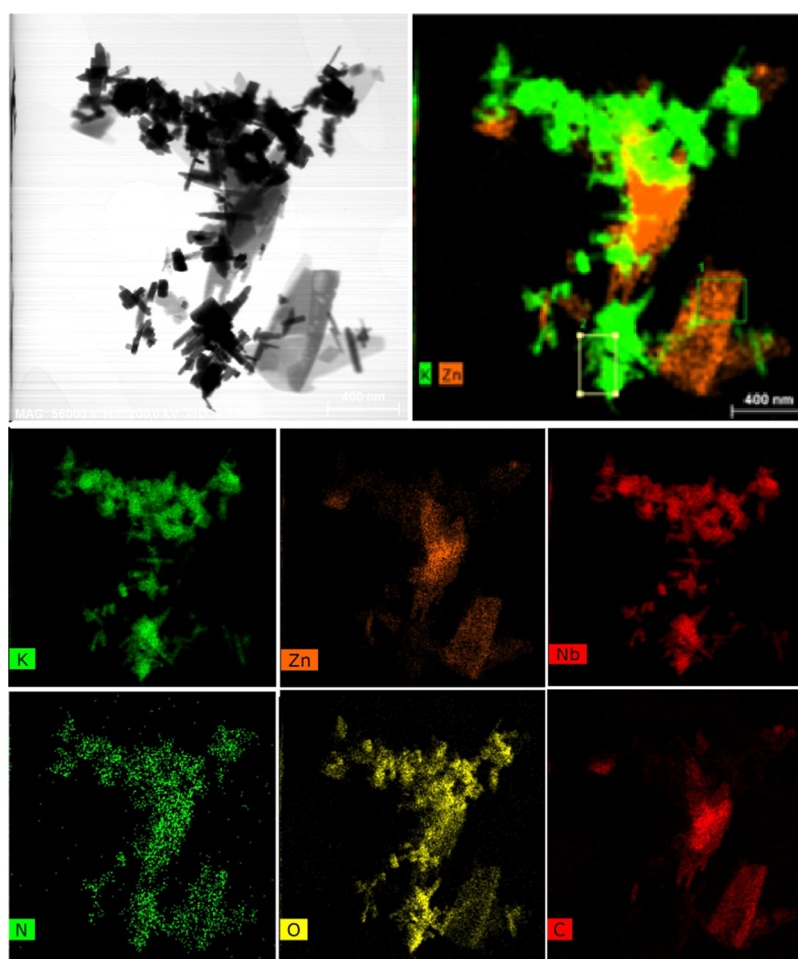


Figure 5. TEM and elemental mapping of $\text{KNbO}_3@TMU-5$.

tion of $\text{KNbO}_3@TMU-5$ and its components. SEM images clearly show that KNbO_3 particles has rod morphology (Figure 4a), while TMU-5 particles are of plate morphology (Figure 4b) in the applied synthesis conditions. These components retain their morphology in the structure of the composite (Figure 4c). TEM elemental mapping images (Figures 5 and S2) display that potassium and niobium elements of KNbO_3 are distributed only on the region of tiny rod particles, while the zinc element, originating from TMU-5, is distributed on

big blocks' region with plate morphology. The superposition of K and Zn reveals better contrast about the posture of TMU-5 blocks (orange color) and KNbO_3 rod particles (green color).

FT-IR spectra of KNbO_3 , TMU-5, and $\text{KNbO}_3@TMU-5$ are depicted in Figure 6. For KNbO_3 , the sharp broad band below 800 cm^{-1} belongs to Nb–O stretching vibration mode. The FT-IR spectrum of the TMU-5 sample shows vibration modes at 1240 and 1160 cm^{-1} related to C–O–C vibrations.²⁵ The weak band at 1299 cm^{-1} and the band ranging from 1320 to

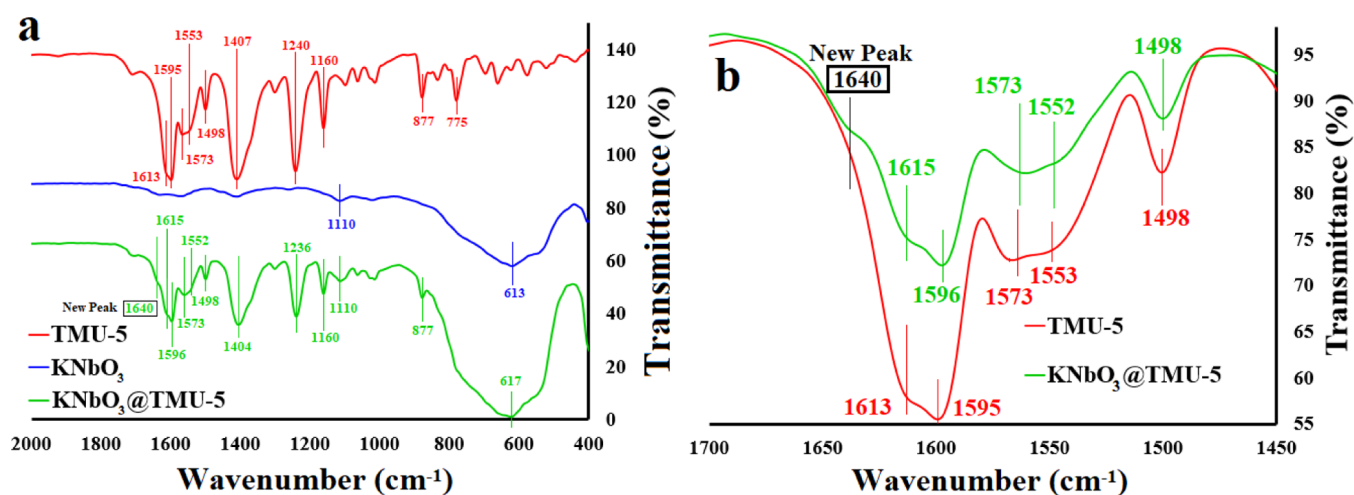


Figure 6. FT-IR spectroscopy for the KNbO₃@TMU-5 composite and its components.

282 1420 cm⁻¹ can be attributed to the asymmetric stretching
 283 mode of C–O bonds. The peak centered at 1498 cm⁻¹ can be
 284 assigned to C=N pyridine stretching vibration. The bands
 285 centered at 1553 and 1573 cm⁻¹ may be due to C=C
 286 stretching vibration modes. The bands at 1613 and 1595 cm⁻¹
 287 are related to C=N–N=C (azine) and C=N (azomethine)
 288 stretching vibration modes, respectively.²⁵ For KNbO₃@
 289 TMU-5, all vibration bands of both KNbO₃ and TMU-5 are
 290 detected with very slight shifts (Figure 6a). Furthermore, a new
 291 vibration band appeared at 1640 cm⁻¹, which may be
 292 attributed to new C=N vibration mode resulting from
 293 interaction between azomethine groups of TMU-5 with the
 294 KNbO₃ structure (Figure 6b).^{26,27} Deconvolution of IR bands
 295 ranging from 1450 to 1700 cm⁻¹ also displays these details
 296 with more clarity (Figure S3).

297 Compared to the XRD technique, Raman spectroscopy is
 298 more sensitive to lattice disorder.¹⁶ Therefore, lattice
 299 perturbations in the local structure of NbO₆ octahedra of
 300 KNbO₃ coupled to TMU-5 were investigated by Raman
 301 spectroscopy. Figure 7 depicts the corresponding Raman
 302 spectra of KNbO₃ and KNbO₃@TMU-5 samples. For KNbO₃,

all the characteristic peaks corresponding to the NbO₆ 303
 octahedra appear at the same pattern of the orthorhombic 304
 phase reported in literature.^{25,27} B1(TO₂), B1(TO₃), A1- 305
 (TO₃), and A1(LO₃) symmetry modes of NbO₆ are observed 306
 at 191.1, 536.9, 594.3, and 834.9 cm⁻¹, respectively. Also, a 307
 broad band comprising three vibrating modes of B1(TO1), 308
 B1(TO4), and A1(TO1) is detected in the 197–298 cm⁻¹ 309
 range.²⁸ The pattern of the orthorhombic phase is also 310
 observed for the KNbO₃@TMU-5 spectrum, while several new 311
 bands are detected above 900 cm⁻¹, which can be related to 312
 TMU-5 structure vibration modes. Furthermore, vibration 313
 modes of the potassium niobate phase detected in the 314
 KNbO₃@TMU-5 Raman spectrum revealed slight shifts, as 315
 compared to the pristine KNbO₃ spectrum. The Raman signal 316
 at 191.1 cm⁻¹, attributed to the internal bending vibration 317
 mode of the NbO₆ octahedron, experienced a slight shift to 318
 192.7 cm⁻¹ for the KNbO₃@TMU-5 sample. Also, the shift of 319
 O–Nb–O symmetric stretching vibration mode of NbO₆ from 320
 591.5 to 589 cm⁻¹ implies its softening due to lowering the 321
 bond force constant.^{28,29} In contrast, no shift was observed for 322
 the band at 536.9 cm⁻¹ ascribed to the stretching vibration 323
 mode of NbO₆.¹⁶ Moreover, the Raman spectrum of KNbO₃@ 324
 TMU-5 is more broadened than that of KNbO₃, suggesting that 325
 the lattice disorder of KNbO₃ is increased upon coupling with 326
 TMU-5. Subsequently, evaluation of Raman spectra suggests 327
 the presence of interaction between the TMU-5 and KNbO₃ 328
 structure in the KNbO₃@TMU-5 sample, which affects NbO₆ 329
 octahedron vibration modes.³⁰ 330

3.2. Photocatalytic Reduction of N₂. The photocatalytic 331
 reduction of N₂ to NH₃ comprises several steps. First, like for 332
 any other photocatalytic reaction, the photocatalyst absorbs 333
 light of appropriate wavelength to generate electron–hole pairs 334
 (eq 1). Afterward, a fraction of the photogenerated electrons 335
 and holes recombine together, while some holes (h⁺) oxidize 336
 water into H⁺ and O₂ (eq 2) and electrons reduce N₂ to NH₃ 337
 (eq 3). Therefore, NH₃ is synthesized from water and N₂ using 338
 light as the energy source (eq 4).² 339

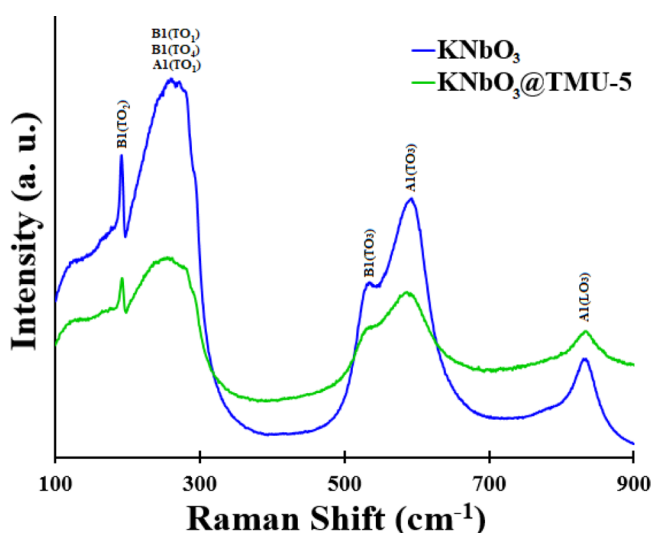
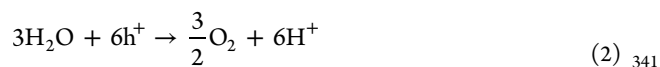
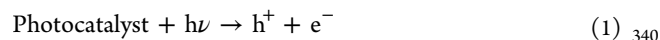
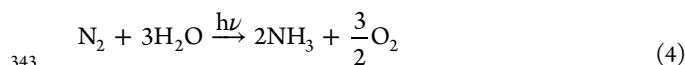


Figure 7. Room-temperature Raman spectra of KNbO₃ (blue) and KNbO₃@TMU-5 (violet) samples.



Even though any photocatalyst having a band gap energy larger than 1.2 eV with proper CB and VB positions can thermodynamically promote the reaction of eq 3, this half-reaction is kinetically more challenging because of the required six electrons. Furthermore, the adsorption of N_2 gas molecules over the photocatalyst surface and cleavage of the highly stable $\text{N}\equiv\text{N}$ bond are also regarded as remarkable challenges.² To address these issues, coupling of the photocatalyst with MOFs having high capacity for N_2 gas molecule adsorption, which can modify the electron transfer mechanism in the photocatalyst, could represent a promising strategy.^{18,31} Apart from enhancement in adsorption capacity, many investigations demonstrated that coupling of a SC with MOFs can modify the electronic structure of the SC, leading to enhanced performance for various photocatalytic reactions including water splitting, CO_2 reduction, and organic pollutant degradation.¹⁸ Nevertheless, for N_2 photo-reduction reaction, there are still a few reports about the role of MOFs in improving the SCs' photocatalytic activity. Hence, for improvement of the operation of KNbO_3 through enhancement in adoption capacity and photocatalytic activity, it has been coupled to TMU-5 to synthesize the $\text{KNbO}_3@TMU-5$ hybrid material.

The photocatalytic activity of the as-synthesized KNbO_3 and $\text{KNbO}_3@TMU-5$ samples for the reduction of N_2 to NH_3 in the presence of water is illustrated in Figure 8. Without light

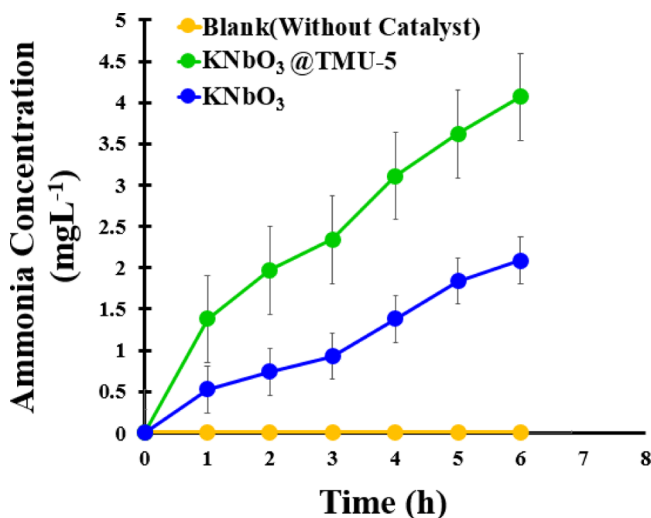


Figure 8. N_2 reduction to ammonia efficiency as a function of irradiation time under UV illumination.

irradiation (blank test), no NH_3 was formed by adding KNbO_3 or $\text{KNbO}_3@TMU-5$ catalysts to N_2 -saturated aqueous solution (Figure S4). Under UV light irradiation, the NH_3 generation rate reaches $20.5 \mu\text{mol}\cdot\text{L}^{-1}\cdot\text{h}^{-1}\cdot\text{g}^{-1}$ in the presence of the KNbO_3 photocatalyst, while by applying $\text{KNbO}_3@TMU-5$, the NH_3 generation rate increased to $39.9 \mu\text{mol}\cdot\text{L}^{-1}\cdot\text{h}^{-1}\cdot\text{g}^{-1}$. To examine the reusability of the $\text{KNbO}_3@TMU-5$ photocatalyst, the N_2 reduction system was recycled five times (Figure 9). During the first three cycles of the reaction, NH_3 production efficiency was not changed. However, after the fifth run, the NH_3 production rate is $37.9 \mu\text{mol}\cdot\text{L}^{-1}\cdot\text{h}^{-1}\cdot\text{g}^{-1}$, confirming the high stability of the developed photocatalyst. Table S1 compares the rate of nitrogen reduction for $\text{KNbO}_3@TMU-$

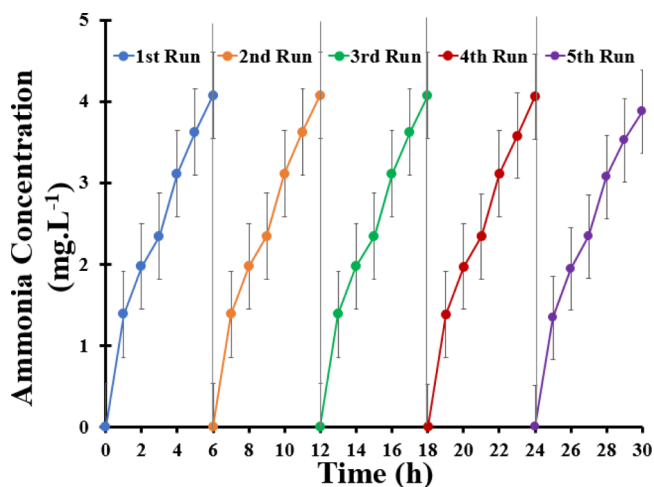


Figure 9. Photocatalytic stability of $\text{KNbO}_3@TMU-5$ during five cycling tests.

5 with some of other MOF-based photocatalysts applied in this area.

To investigate the effect of coupling of TMU-5 on the charge transfer and recombination behavior of KNbO_3 , photoluminescence measurements were employed at an excitation wavelength of 325 nm. As shown in Figure S5, the KNbO_3 sample exhibited a strong blue luminescence emission in the 350–455 nm range, which may be attributed to the emission connected with charge transfer from oxygen atoms to the central niobium atom in the NbO_6 octahedra. The luminescence emission was observed for the $\text{KNbO}_3@TMU-5$ sample with relatively lower intensity compared to pristine KNbO_3 , suggesting that TMU-5 hybridization with KNbO_3 reduces the recombination rate of photogenerated electron-hole pairs, which may be due to the internal charge transfer between the KNbO_3 and TMU-5 component.³² A complementary study on electron-hole separation by photocurrent measurement demonstrates that the rate of charge recombination is significantly diminished upon hybridization of KNbO_3 with TMU-5 (Figure S6). These results clearly show that the photoactivity of the $\text{KNbO}_3@TMU-5$ composite is highly improved compared to pristine KNbO_3 .

To investigate the effect of TMU-5 on the optical properties of KNbO_3 , UV-vis analysis was performed (Figure S7). The optical band gap ($E(\text{bg})$) of KNbO_3 and $\text{KNbO}_3@TMU-5$ samples was determined using the following equation (eq 5):

$$(\alpha h\nu)^n = A(h\nu - E(\text{bg})) \quad (5)$$

where α , h , ν , A , and $E(\text{bg})$ represent the absorption coefficient, Planck constant, light frequency, proportionality constant, and band gap, respectively. The value of n depends on the nature of the electronic transition and assumed to be 1/2 for KNbO_3 , which has an indirect band gap. By plotting $(\alpha h\nu)^{1/2}$ versus $(h\nu)$, $E(\text{bg})$ can be estimated from the intercept of the tangent to the x -axis.²⁸ Accordingly, an $E(\text{bg})$ value of 3.2 eV (387.45 nm) was calculated for KNbO_3 , which is in good agreement with previous reports.^{28,33} After hybridization of KNbO_3 with TMU-5, the $E(\text{bg})$ value decreased slightly to 3.1 eV (399.95 nm).

In the next step, the Mott-Schottky diagram has been drawn to calculate the flat band potentials ($E(\text{fb})$) of TMU-5 and KNbO_3 components to calculate their CB and VB energy levels (Figure S8). The calculated $E(\text{fb})$ values for TMU-5 and

424 KNbO_3 are -1.4 V and -0.7 V, respectively. In a general
 425 verified approximation for n-type photocatalysts, energy levels
 426 of CB and VB can be calculated based on following equations
 427 (eqs 6 and 7).

$$428 \quad E_{\text{CB}} = E(\text{fb}) - 0.2 \quad (6)$$

$$429 \quad E_{\text{VC}} = E_{\text{CB}} + E(\text{bg}) \quad (7)$$

430 According to the values of $E(\text{fb})$ and $E(\text{bg})$ for TMU-5 and
 431 KNbO_3 (Table S2), the mechanistic diagram of photo-
 432 reduction of nitrogen by $\text{KNbO}_3@TMU-5$ is depicted in
 433 Figure 10.

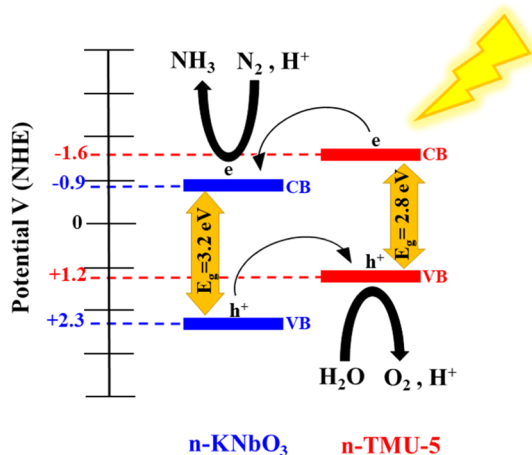


Figure 10. Energy levels of TMU-5 and KNbO_3 and mechanism of nitrogen reduction by $\text{KNbO}_3@TMU-5$.

434 **3.3. Mechanism of Nitrogen Reduction.** XPS analysis is
 435 an ideal technique for characterization of a material before and
 436 after coupling with another component in a composite. In this
 437 regard, XPS analysis applied to understand the electronic state
 438 of the KNbO_3 atoms before and after coupling with TMU-5.
 439 The core-level XPS spectra for Zn, C, K, and O and especially
 440 Nb and N atoms were collected.

441 The core-level spectra of Zn 2p of TMU-5 and $\text{KNbO}_3@$
 442 TMU-5 are displayed in Figure S9. The Zn 2p spectrum of
 443 TMU-5 contains a doublet at binding energies (BEs) of 1019.3
 444 and 1042.4 eV assigned to $\text{Zn}2p_{3/2}$ and $\text{Zn}2p_{1/2}$ lines,
 445 respectively.¹⁹ These values observed in case of $\text{KNbO}_3@$
 446 TMU-5, too.

447 The core-level scans of the C 1s of KNbO_3 , TMU-5, and
 448 $\text{KNbO}_3@TMU-5$ samples are illustrated in Figure S10. A sharp
 449 peak for the KNbO_3 sample situated at 284.9 eV is observed
 450 and can be assigned to the adventitious carbon. For TMU-5,
 451 the spectrum can be curve-fitted by three components at 284.9,
 452 286.2, and 288.6 eV ascribed respectively to the sp^2 -hybridized
 453 carbon including aromatic carbon ($-\text{C}=\text{C}$), carbon-nitrogen
 454 or carbon-oxygen bonds, and ($\text{O}-\text{C}=\text{O}$) bonds.³⁴ The C 1s
 455 spectrum of the $\text{KNbO}_3@TMU-5$ sample is also deconvoluted
 456 into three peaks at 284.9 eV ($\text{C}=\text{C}$), 285.8 eV ($\text{C}-\text{N}/\text{C}-\text{O}$),
 457 and 288.6 ($\text{O}-\text{C}=\text{O}$) eV.

458 For the KNbO_3 sample, the BEs of K 2p_{3/2} and K2p_{1/2},
 459 illustrated in Figure S11, are close to 291.0 and 293.7 eV,
 460 respectively. A positive shift (0.7 eV) is observed for the
 461 $\text{KNbO}_3@TMU-5$ sample that can be due to the decrease of
 462 potassium electron density after coupling of KNbO_3 to TMU-
 463 5.³⁵

Based on XPS measurements (Figure 11), Nb 3d_{5/2} and Nb 3d_{3/2} of KNbO_3 are located at 206.5 and 209.3 eV, 464 f11 465

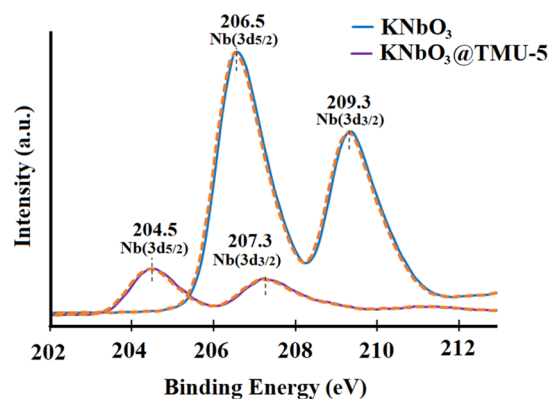


Figure 11. Core-level XPS scan of Nb atoms for KNbO_3 and $\text{KNbO}_3@TMU-5$.

respectively, with a spin-orbit splitting of 2.8 eV. After
 466 hybridization of TMU-5 with KNbO_3 , the Nb 3d_{5/2} and Nb
 467 3d_{3/2} core-level binding energies (BEs) shifted to 204.5 and
 468 207.3, respectively. According to the literature, this negative
 469 shift can be ascribed to electron transfer to Nb atoms.³⁶ 470

As shown in Figure 12, for the TMU-5 sample, the N 1s XPS
 471 sharp peak can be fitted to the C=N group (397.9 eV). The
 472 C=N peak is shifted to 397.1 eV in the $\text{KNbO}_3@TMU-5$
 473 hybrid material.³⁴ The weak peaks centered at 399.2 eV for
 474 both TMU-5 and $\text{KNbO}_3@TMU-5$ samples can be ascribed to
 475 pyridine nitrogen of the BPDH ligand of TMU-5. These results
 476 show that upon formation of the $\text{KNbO}_3@TMU-5$ composite,
 477 the electronic properties of N atoms of coordinating pyridine
 478 groups did not change, while an alteration in electronic
 479 properties of N atoms of azine function ($-\text{C}=\text{N}-\text{N}=\text{C}-$) is
 480 observed. 481

The O 1s XPS spectra of KNbO_3 and $\text{KNbO}_3@TMU-5$ are
 482 displayed in Figure S12. For KNbO_3 , the spectrum can be
 483 deconvoluted into three components at 529.4, 530.2, and
 484 531.7 eV due to oxygen of perovskite lattice, oxygen deficient
 485 bonding, and weakly bound O^- and OH^- surface species,
 486 respectively (Figure S12a). The O 1s XPS spectrum of TMU-5
 487 is fitted with two components at 529.8 and 531.4 eV, which
 488 can be assigned to carboxylate and ether groups of the OBA²⁻
 489 ligand of TMU-5, respectively (Figure S12b). The spectrum of
 490 the $\text{KNbO}_3@TMU-5$ sample can be curve-fitted with four
 491 components at 527.2, 529.2, 531.1, and 531.9 eV (Figure
 492 S12c).³⁷ Compared to O 1s XPS spectra of KNbO_3 and TMU-
 493 5 samples, a new peak centered at 527.2 eV (O^* atom in
 494 Figure S12c) is observed for $\text{KNbO}_3@TMU-5$. 495

Overall, based on the observed shifts in XPS analysis of
 496 TMU-5 and KNbO_3 samples before and after hybridization in
 497 the $\text{KNbO}_3@TMU-5$ composite, it is possible to say that the
 498 significant changes in oxidation numbers are observed in the
 499 case of Nb and N atoms. These changes are discussed in detail
 500 as follows. For this purpose, the required information from FT-
 501 IR and XPS analyses is gathered here and discussed together. 502

As is mentioned, Nb(3d) core-level XPS analysis shows that
 503 the BE for Nb atoms shifts is equal to 2 eV after synthesis of
 504 $\text{KNbO}_3@TMU-5$, while the value of spin-orbit coupling (2.8
 505 eV) does not alter. Because such a shift in the BE of Nb atoms
 506 occurs after hybridization of KNbO_3 with TMU-5, it is rational
 507 to hypothesize that there is some kind of interactions between 508

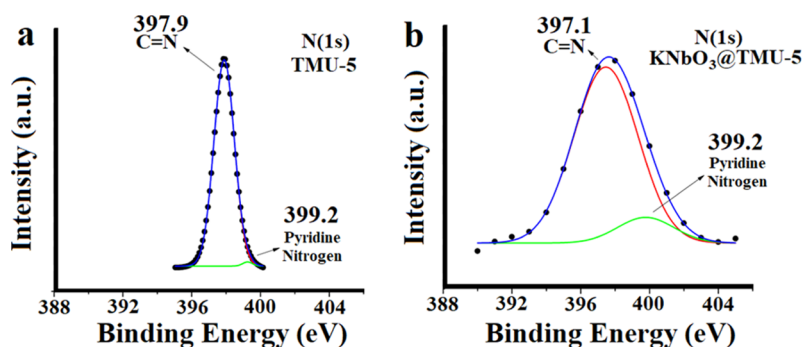


Figure 12. Core-level XPS scan of N atoms for TMU-5 (a) and $\text{KNbO}_3@TMU-5$ (b).

509 these two materials in the final composite. Based on N(1s)
 510 core-level XPS, it has been observed that there is a positive
 511 shift equal to 0.8 eV in the BE of the azine $-\text{C}=\text{N}-$ site, while
 512 the binding energy of pyridine $-\text{C}=\text{N}-$ is completely
 513 unchanged. Based on core-level XPS analysis of N and Nb
 514 atoms, it is possible to state that Nb sites of KNbO_3 and azine
 515 functions ($-\text{C}=\text{N}-\text{N}=\text{C}-$) of TMU-5 are potential
 516 interactive sites after the formation of the $\text{KNbO}_3@TMU-5$
 517 photocatalyst.

518 The mentioned assumption, possible interaction between
 519 Nb^{+5} centers and azine sites in the composite, can be witnessed
 520 using FT-IR spectroscopy specifically in the $1450-1700\text{ cm}^{-1}$
 521 region. Based on the literature, this region belongs to
 522 observation of $-\text{C}=\text{N}-$ bonds. As can be seen in Figure
 523 6b, there is a new peak centered at 1640 cm^{-1} after the
 524 formation of the $\text{KNbO}_3@TMU-5$ composite, while other
 525 peaks (related to pyridine $\text{C}=\text{N}$, aromatic $\text{C}=\text{C}$, azomethine
 526 $-\text{C}=\text{N}-$ and azine $-\text{C}=\text{N}-\text{N}=\text{C}-$ bonds) are almost
 527 identical. According to the literature, FT-IR analysis of
 528 aromatic azine function shows a singlet peak at the $1600-$
 529 1635 cm^{-1} region,³⁸ similar to what we observed here, 1613
 530 cm^{-1} for TMU-5 and 1615 cm^{-1} for the composite. In the
 531 cases that there is a specific interaction between azine $-\text{C}=\text{N}-$
 532 $\text{N}-\text{N}=\text{C}-$ bonds and metal, a new peak can be observed in
 533 the $1630-1652\text{ cm}^{-1}$ region.³⁹ Therefore, according to shifts
 534 in XPS peaks of Nb atoms along with the formation of a new
 535 band at 1640 cm^{-1} in FT-IR, we reason that there is specific
 536 kind of interaction between azine functions of TMU-5 and
 537 Nb^{+5} sites of KNbO_3 in the composite. Based on principles of
 538 XPS measurement, the BE of a specific atom will decrease if
 539 the density of negative charges is increased on that specific
 540 atom. Therefore, due to the shift in the BE of Nb^{+5} sites to the
 541 lower values, it can be speculated that the density of negative
 542 charges is increased on Nb^{+5} sites. The final values of BE of Nb
 543 sites in the composite is relatively similar to Nb^{+4} species
 544 published in the literature.⁴⁰⁻⁴² This higher negative charge
 545 density on Nb sites is another reason for improvement of N_2
 546 reduction efficiency in case of $\text{KNbO}_3@TMU-5$ compared to
 547 pristine KNbO_3 . Cyclic voltammetry has been conducted to
 548 compare the reducing strength of KNbO_3 before and after
 549 hybridization (Figure S13). The results show that the
 550 reduction reaction on $\text{KNbO}_3@TMU-5$ shifts to more positive
 551 reduction potentials as equal as 60 mV (from -770 to -710
 552 mV), which indicates that the $\text{KNbO}_3@TMU-5$ composite has
 553 higher affinity to reduction reactions compared to KNbO_3 .

554 Therefore, $\text{KNbO}_3@TMU-5$ is a more efficient photo-
 555 catalyst for reductive photoconversion of nitrogen molecules to
 556 ammonia. Overall, there are three major reasons that assist
 557 $\text{KNbO}_3@TMU-5$ to show higher efficiency compared to

pristine KNbO_3 , which are (I) increased porosity and surface
 558 area, (II) higher efficiency in photoinduced electron-hole
 559 separation, and (III) higher density of negative charges on Nb
 560 sites in the composite. Based on these reasons, the mechanism
 561 of nitrogen photoreduction by $\text{KNbO}_3@TMU-5$ can be
 562 described in detail as follows. In the first step, N_2 molecules
 563 access the surface of KNbO_3 through diffusion in the three-
 564 dimensional interconnected pores of TMU-5. In this
 565 condition, it can be stated that the pores of TMU-5 act as
 566 nanocylinders to accumulate the surface of KNbO_3 with
 567 nitrogen molecules. Due to the higher surface area of
 568 $\text{KNbO}_3@TMU-5$ than pristine KNbO_3 , it is anticipated that
 569 the concentration of N_2 molecules on the surface of KNbO_3 is
 570 more than that on pristine KNbO_3 . In the next step, upon light
 571 irradiation, the organic framework of TMU-5 is used as
 572 antenna and absorbs light photons, which improves the
 573 electron-hole separation efficiency of $\text{KNbO}_3@TMU-5$,
 574 becoming higher than that of pristine KNbO_3 . The higher
 575 the charge carrier separation, the higher will be the
 576 photocatalytic efficiency. In the final step, it is anticipated
 577 that the rate of N_2 reduction will increase due to the changes in
 578 BEs and higher affinity of Nb sites to the reduction reaction in
 579 the composite after hybridization of KNbO_3 with TMU-5 in
 580 the composite. Therefore, the rate of ammonia production will
 581 increase for KNbO_3 in the composite form when compared to
 582 the pristine form. 583

CONCLUSIONS 584

KNbO_3 is one of the perovskite-based SCs that was used for
 585 photocatalytic nitrogen reduction. However, it has some
 586 disadvantages like no porosity and band gap in the UV region.
 587 To overcome these challenges, we have synthesized a hybrid
 588 material based on KNbO_3 and one of our TMU MOFs named
 589 as TMU-5 because it is porous to nitrogen molecules and its
 590 optical band gap lies in the visible region. Experimental
 591 analyses suggest that there are three reasons for improved
 592 photocatalytic activity of KNbO_3 in the $\text{KNbO}_3@TMU-5$
 593 composite when compared to the pristine material. The higher
 594 surface area and porosity of the composite compared to
 595 pristine KNbO_3 , higher affinity of Nb sites to reduction
 596 reaction in the composite due to the changes in BEs after
 597 hybridization, and higher efficiency in electron-hole separa-
 598 tion in the composite are the major reasons for improved
 599 photocatalytic activity of the $\text{KNbO}_3@TMU-5$ composite
 600 when compared to pristine KNbO_3 . 601

602 ■ ASSOCIATED CONTENT

603 ■ Supporting Information

604 The Supporting Information is available free of charge at
605 <https://pubs.acs.org/doi/10.1021/acs.inorgchem.1c03622>.

606 TMU-5 framework scheme, TEM images, deconvoluted
607 FT-IR spectrum, blank photocatalytic tests, photo-
608 luminescence and photocurrent measurements, Tauc
609 plots, Mott–Schottky diagrams, and XPS measurements
610 (PDF)

611 ■ AUTHOR INFORMATION

612 Corresponding Authors

613 Ali Morsali – Department of Chemistry, Faculty of Sciences,
614 Tarbiat Modares University, Tehran 14117-13116, Islamic
615 Republic of Iran; orcid.org/0000-0002-1828-7287;
616 Phone: (+98) 21-82884416; Email: morsali_a@modares.ac.ir

617 modares.ac.ir
618 Afshanehsadat Larimi – Department of Chemical and Process
619 Engineering, Niroo Research Institute, Tehran 14686-13113,
620 Iran; orcid.org/0000-0001-5566-171X;
621 Email: Alarimi@nri.ac.ir

622 Rabah Boukherroub – University of Lille, CNRS, Centrale
623 Lille, Université Polytechnique Hauts-de-France, UMR 8520,
624 IEMN, Lille F-59000, France; Email: rabah.boukherroub@univ-lille.fr

626 Authors

627 Masoumeh Chamack – Department of Chemistry, Faculty of
628 Sciences, Tarbiat Modares University, Tehran 14117-13116,
629 Islamic Republic of Iran

630 Madjid Ifires – University of Lille, CNRS, Centrale Lille,
631 Université Polytechnique Hauts-de-France, UMR 8520,
632 IEMN, Lille F-59000, France; Research Center of Semi-
633 conductor Technology for Energy, Merveilles 16038, Algeria

634 Sayed Ali Akbar Razavi – Department of Chemistry, Faculty
635 of Sciences, Tarbiat Modares University, Tehran 14117-
636 13116, Islamic Republic of Iran

637 Ahmed Addad – University of Lille, CNRS, UMR 8207—
638 UMET, Lille F-59000, France

639 Sabine Szunerits – University of Lille, CNRS, Centrale Lille,
640 Université Polytechnique Hauts-de-France, UMR 8520,
641 IEMN, Lille F-59000, France; orcid.org/0000-0002-1567-4943

643 Complete contact information is available at:

644 <https://pubs.acs.org/doi/10.1021/acs.inorgchem.1c03622>

645 Notes

646 The authors declare no competing financial interest.

647 ■ ACKNOWLEDGMENTS

648 National Centre for Scientific Research (CNRS), Center for
649 International Scientific Studies and Collaboration (CISS), The
650 University of Lille, the Hauts-de-France region, Tarbiat
651 Modares University (TMU), and Niroo Research Institute
652 (NRI) are gratefully acknowledged for financial support.

653 ■ REFERENCES

654 (1) Chen, X.; Li, N.; Kong, Z.; Ong, W.-J.; Zhao, X. Photocatalytic
655 fixation of nitrogen to ammonia: state-of-the-art advancements and
656 future prospects. *Mater. Horiz.* **2018**, *5*, 9–27.

(2) Vu, M.-H.; Sakar, M.; Do, T.-O. Insights into the recent progress
and advanced materials for photocatalytic nitrogen fixation for
ammonia (NH₃) production. *Catalysts* **2018**, *8*, 621.

(3) Shi, R.; Zhao, Y.; Waterhouse, G. I. N.; Zhang, S.; Zhang, T.
Defect engineering in photocatalytic nitrogen fixation. *ACS Catal.*
2019, *9*, 9739–9750.

(4) Chen, S.; Liu, D.; Peng, T. Fundamentals and Recent Progress of
Photocatalytic Nitrogen-Fixation Reaction over Semiconductors. *Sol.*
RRL **2021**, *5*, 2000487.

(5) Comer, B. M.; Medford, A. J. Analysis of photocatalytic nitrogen
fixation on rutile TiO₂ (110). *ACS Sustainable Chem. Eng.* **2018**, *6*,
4648–4660.

(6) Kumar, A.; Kumar, A.; Krishnan, V. Perovskite oxide based
materials for energy and environment-oriented photocatalysis. *ACS*
Catal. **2020**, *10*, 10253–10315.

(7) Xing, P.; Wu, S.; Chen, Y.; Chen, P.; Hu, X.; Lin, H.; Zhao, L.;
He, Y. New application and excellent performance of Ag/KNbO₃
nanocomposite in photocatalytic NH₃ synthesis. *ACS Sustainable*
Chem. Eng. **2019**, *7*, 12408–12418.

(8) Xing, P.; Zhang, W.; Chen, L.; Dai, X.; Zhang, J.; Zhao, L.; He,
Y. Preparation of a NiO/KNbO₃ nanocomposite via a photo-
deposition method and its superior performance in photocatalytic N₂
fixation. *Sustain. Energy Fuels* **2020**, *4*, 1112–1117.

(9) Zhang, H.; Li, X.; Su, H.; Chen, X.; Zuo, S.; Yan, X.; Liu, W.;
Yao, C. Sol–gel synthesis of upconversion perovskite/attapulgite
heterostructures for photocatalytic fixation of nitrogen. *J. Sol-Gel Sci.*
Technol. **2019**, *92*, 154–162.

(10) Tao, R.; Li, X.; Li, X.; Shao, C.; Liu, Y. TiO₂/SrTiO₃/gC₃N₄
ternary heterojunction nanofibers: gradient energy band, cascade
charge transfer, enhanced photocatalytic hydrogen evolution, and
nitrogen fixation. *Nanoscale* **2020**, *12*, 8320–8329.

(11) Mansingh, S.; Sultana, S.; Acharya, R.; Ghosh, M. K.; Parida, K.
Efficient photon conversion via double charge dynamics CeO₂–
BiFeO₃ p–n heterojunction photocatalyst promising toward N₂
fixation and phenol–Cr (VI) detoxification. *Inorg. Chem.* **2020**, *59*,
3856–3873.

(12) Li, X.; He, C.; Dai, D.; Zuo, S.; Yan, X.; Yao, C.; Ni, C. Nano-
mineral induced nonlinear optical LiNbO₃ with abundant oxygen
vacancies for photocatalytic nitrogen fixation: boosting effect of
polarization. *Appl. Nanosci.* **2020**, *10*, 3477–3490.

(13) Zhang, C.; Chen, G.; Lv, C.; Yao, Y.; Xu, Y.; Jin, X.; Meng, Q.
Enabling nitrogen fixation on Bi₂WO₆ photocatalyst by c-PAN
surface decoration. *ACS Sustainable Chem. Eng.* **2018**, *6*, 11190–
11195.

(14) Zhou, S.; Zhang, C.; Liu, J.; Liao, J.; Kong, Y.; Xu, Y.; Chen, G.
Formation of an oriented Bi₂WO₆ photocatalyst induced by in situ
Bi reduction and its use for efficient nitrogen fixation. *Catal. Sci.*
Technol. **2019**, *9*, 5562–5566.

(15) Shi, H.; Zhang, C.; Zhou, C.; Chen, G. Conversion of CO₂
into renewable fuel over Pt–gC₃N₄/KNbO₃ composite
photocatalyst. *RSC Adv.* **2015**, *5*, 93615–93622.

(16) Zhang, T.; Zhao, K.; Yu, J.; Jin, J.; Qi, Y.; Li, H.; Hou, X.; Liu,
G. Photocatalytic water splitting for hydrogen generation on cubic,
orthorhombic, and tetragonal KNbO₃ microcubes. *Nanoscale* **2013**,
5, 8375–8383.

(17) Liu, J.; Li, R.; Zu, X.; Zhang, X.; Wang, Y.; Wang, Y.; Fan, C.
Photocatalytic conversion of nitrogen to ammonia with water on
triphasic interfaces of hydrophilic-hydrophobic composite Bi₄O₅Br₂/
ZIF-8. *Chem. Eng. J.* **2019**, *371*, 796–803.

(18) Huang, C.-W.; Nguyen, V.-H.; Zhou, S.-R.; Hsu, S.-Y.; Tan, J.-
X.; Wu, K. C.-W. Metal–organic frameworks: preparation and
applications in highly efficient heterogeneous photocatalysis. *Sustain.*
Energy Fuels **2020**, *4*, 504–521.

(19) Abazari, R.; Morsali, A.; Dubal, D. P. An advanced composite
with ultrafast photocatalytic performance for the degradation of
antibiotics by natural sunlight without oxidizing the source over
TMU-5@ Ni–Ti LDH: mechanistic insight and toxicity assessment.
Inorg. Chem. Front. **2020**, *7*, 2287–2304.

- 725 (20) Bagheri, M.; Masoomi, M. Y.; Morsali, A. A MoO₃–Metal–
726 Organic Framework Composite as a Simultaneous Photocatalyst and
727 Catalyst in the PODS Process of Light Oil. *ACS Catal.* **2017**, *7*,
728 6949–6956.
- 729 (21) Masoomi, M. Y.; Stylianou, K. C.; Morsali, A.; Retailleau, P.;
730 Maspoch, D. Selective CO₂ Capture in Metal–Organic Frameworks
731 with Azine-Functionalized Pores Generated by Mechanochemistry.
732 *Cryst. Growth Des.* **2014**, *14*, 2092–2096.
- 733 (22) Yuan, B.; Ma, D.; Wang, X.; Li, Z.; Li, Y.; Liu, H.; He, D. A
734 microporous, moisture-stable, and amine-functionalized metal–
735 organic framework for highly selective separation of CO₂ from
736 CH₄. *Chem. Commun.* **2012**, *48*, 1135–1137.
- 737 (23) Zhu, D.; Zhang, L.; Ruther, R. E.; Hamers, R. J. Photo-
738 illuminated diamond as a solid-state source of solvated electrons in
739 water for nitrogen reduction. *Nat. Mater.* **2013**, *12*, 836–841.
- 740 (24) Thommes, M.; Kaneko, K.; Neimark, A. V.; Olivier, J. P.;
741 Rodriguez-Reinoso, F.; Rouquerol, J.; Sing, K. S. Physisorption of
742 gases, with special reference to the evaluation of surface area and pore
743 size distribution (IUPAC Technical Report). *Pure Appl. Chem.* **2015**,
744 *87*, 1051–1069.
- 745 (25) Kulaksızoğlu, S.; Gup, R. A new bis (azine) tetradentate ligand
746 and its transition metal complexes: Synthesis, characterisation, and
747 extraction properties. *Chem. Pap.* **2012**, *66*, 194–201.
- 748 (26) Clougherty, L.; Sousa, J.; Wyman, G. C= N stretching
749 frequency in infrared spectra of aromatic azomethines. *J. Org. Chem.*
750 **1957**, *22*, 462.
- 751 (27) Stratton, W. J.; Busch, D. H. The Complexes of
752 Pyridinaldazine. III. Infrared Spectra and Continued Synthetic
753 Studies. *J. Am. Chem. Soc.* **1960**, *82*, 4834–4839.
- 754 (28) Golovina, I. S.; Bryksa, V. P.; Strelchuk, V. V.; Geifman, I. N.;
755 Andriiko, A. A. Size effects in the temperatures of phase transitions in
756 KNbO₃ nanopowder. *J. Appl. Phys.* **2013**, *113*, 144103.
- 757 (29) Pascual-Gonzalez, C.; Schileo, G.; Khesro, A.; Sterianou, I.;
758 Wang, D.; Reaney, I. M.; Feteira, A. Band gap evolution and a
759 piezoelectric-to-electrostrictive crossover in (1–x) KNbO₃–x (Ba
760 0.5 Bi 0.5)(Nb 0.5 Zn 0.5) O₃ ceramics. *J. Mater. Chem. C* **2017**, *5*,
761 1990–1996.
- 762 (30) Jia, S.; Su, Y.; Zhang, B.; Zhao, Z.; Li, S.; Zhang, Y.; Li, P.; Xu,
763 M.; Ren, R. Few-layer MoS₂ nanosheet-coated KNbO₃ nanowire
764 heterostructures: piezo-photocatalytic effect enhanced hydrogen
765 production and organic pollutant degradation. *Nanoscale* **2019**, *11*,
766 7690–7700.
- 767 (31) Zhao, S.-N.; Wang, G.; Poelman, D.; Van Der Voort, P. Metal
768 organic frameworks based materials for heterogeneous photocatalysis.
769 *Molecules* **2018**, *23*, 2947.
- 770 (32) Shi, W.; Shu, K.; Huang, X.; Ren, H.; Li, M.; Chen, F.; Guo, F.
771 Enhancement of visible-light photocatalytic degradation performance
772 over nitrogen-deficient g-C₃N₄/KNbO₃ heterojunction photocata-
773 lyst. *J. Chem. Technol. Biotechnol.* **2020**, *95*, 1476–1486.
- 774 (33) H. Khorrami, G.; Kompany, A.; Khorsand Zak, A. Structural
775 and optical properties of (K, Na) NbO₃ nanoparticles synthesized by
776 a modified sol–gel method using starch media. *Adv. Powder Technol.*
777 **2015**, *26*, 113–118.
- 778 (34) Shalom, M.; Ressnig, D.; Yang, X.; Clavel, G.; Fellingner, T. P.;
779 Antonietti, M. Nickel nitride as an efficient electrocatalyst for water
780 splitting. *J. Mater. Chem. A* **2015**, *3*, 8171–8177.
- 781 (35) Maneerung, T.; Hidajat, K.; Kawi, S. K-doped LaNiO₃
782 perovskite for high-temperature water-gas shift of reformate gas:
783 Role of potassium on suppressing methanation. *Int. J. Hydrogen Energy*
784 **2017**, *42*, 9840–9857.
- 785 (36) Yu, J.; Chen, Z.; Wang, Y.; Ma, Y.; Feng, Z.; Lin, H.; Wu, Y.;
786 Zhao, L.; He, Y. Synthesis of KNbO₃/gC₃N₄ composite and its
787 new application in photocatalytic H₂ generation under visible light
788 irradiation. *J. Mater. Sci.* **2018**, *53*, 7453–7465.
- 789 (37) Ji, Q.; Bi, L.; Zhang, J.; Cao, H.; Zhao, X. S. The role of oxygen
790 vacancies of ABO₃ perovskite oxides in the oxygen reduction
791 reaction. *Energy Environ. Sci.* **2020**, *13*, 1408–1428.
- (38) Frederickson, L. D. An Infrared Study of the C= N Stretching
792 Vibration in Azine Derivatives of Aldehydes and Ketones. *Anal. Chem.* **1964**, *36*, 1349–1355. 794
- (39) Adhikari, S.; Kaminsky, W.; Kollipara, M. R. Pyridyl azine
795 Schiff-base ligands exhibiting unexpected bonding modes towards
796 ruthenium, rhodium and iridium half-sandwich complexes: synthesis
797 and structural studies. *J. Organomet. Chem.* **2017**, *836–837*, 8–16. 798
- (40) Lianwei, S.; Xianyou, Z. XPS study on barium lanthanum
799 magnesium niobate. *J. Rare Earths* **2006**, *24*, 310–313. 800
- (41) Dong, C.; Wang, X.; Liu, X.; Yuan, X.; Dong, W.; Cui, H.;
801 Duan, Y.; Huang, F. In situ grown Nb 4 N 5 nanocrystal on nitrogen-
802 doped graphene as a novel anode for lithium ion battery. *RSC Adv.* **2016**, *6*, 81290–81295. 804
- (42) Wang, J.; Wang, X.; Cui, Z.; Liu, B.; Cao, M. One-pot synthesis
805 and Nb 4 N 5 surface modification of Nb 4+ self-doped KNbO₃
806 nanorods for enhanced visible-light-driven hydrogen production. *Phys.* **2015**, *17*, 14185–14192. 807
808